Changes in Mn^{3+}/Mn^{4+} ratio, resistance values in electrochemical impedance spectra, and rate capability with increased lithium content in spinel $Li_xMn_2O_4$

Yang Fu[a], Yi-Jie Gu[a,*], Yun-Bo Chen[b], Hong-Quan Liu[a], Heng-Hui Zhou[c,*]

[a] College of Materials Science and Engineering, Shandong University of Science and Technology, Qingdao 266510, China
[b] Advanced Manufacture Technology Center, China Academy of Machinery Science and Technology, Beijing 100044, China
[c] College of Chemistry and Molecular Engineering, Peking University, Beijing 100871, China

ARTICLE INFO

ABSTRACT

Spinel-structured $Li_xMn_2O_4$ (x = 1.0, 1.02, 1.04, and 1.06) cathode materials have been synthesized by a solid-state method using Mn_3O_4 and Li_2CO_3 as raw materials. The Mn^{4+} content gradually decreases from 84.80% to 82.62% and then increases from 82.62% to 88.98%, when the Li content increases from 1.00 to 1.06. The rate capability of the $LiMn_2O_4$ samples evidently increases as the lithium content increases from 1.00 to 1.06. Electrochemical impedance spectroscopy results indicate that the R_{ct} values gradually increase from 58.33 Ω to 133.1 Ω and then decrease from 133.1 Ω to 68.79 Ω when the Li concentration increases from 1.00 to 1.06. The R_{sf} values also increase from 25.67 Ω to 37.84 Ω and then decrease from 37.84 Ω to 16.69 Ω, when the Li concentration increases from 1.00 to 1.06. These changes in Mn^{4+} content, R_{sf}, and R_{ct} with the increase in Li content are related to changes in the second phase in $LiMn_2O_4$.

1. Introduction

Nowadays, an increasing number of researchers are paying attention to lithium-ion batteries, which are an important power source for portable electronic devices [1]. Lithium-ion batteries have many advantages such as a high capacity, which is the main reason for their widespread use in hybrid electric vehicles (HEVs) [2–4]. Many studies report the development of $LiMn_2O_4$ as cathode materials that have high specific energy, small self-discharge, and good safety features, in addition to being low cost and environmentally friendly [5]. However, many factors cause capacity fading, such as structural instability induced by the Jahn-Teller distortion and manganese dissolution via the Mn^{3+} disproportion reaction ($2\,Mn^{3+} \rightarrow Mn^{4+} + Mn^{2+}$) [6–9]. There are many reports in literature about Mn^{3+}, Mn^{4+} and $Li_xMn_2O_4$: Shin and Manthiram [10] showed that the capacity fading in LMO is due to the development of microstrains and large differences in the lattice parameters between the two cubic phases during charging. Chung and Kim [11] showed that the onset of Jahn-Teller effects in deeply discharged $Li_xMn_2O_4$ electrodes with a Mn^{3+} rich region on the surface is

the primary cause of the fading. Das and Fachini [12] showed that the capacity fading is attributed to the formation of a strong, passive, fluoride layer on the surface of the film, which led to uncertainty regarding the presence of the Jahn-Teller-active Mn^{3+} in LMO cathodes. Recently, Kang et al. [13] pointed out that Mn^{4+} in a MnO_2 coating layer could not only suppress Mn dissolution effectively, but also provide chemical stability, thereby improving the storage and rate capability of MnO_2-coated $LiMn_2O_4$. Furthermore, Han et al. [14] confirmed that the Mn^{4+}-rich phase is an appropriate candidate for modifying surfaces to suppress the dissolution of Mn, thereby improving the electrochemical properties of $LiMn_2O_4$. Therefore, the presence of Mn^{4+} on the surface of $LiMn_2O_4$ particles can considerably reduce the dissolution of Mn and maintain the stability of $LiMn_2O_4$, resulting in enhanced electrochemical performance.

High-rate discharge capability is another important factor to be considered in high-power batteries. Doping of metal cations and anions with small radii, such as F^- and S^{2-}, could improve the high-rate discharge capability of spinel $LiMn_2O_4$ [15–17]. In our previous study, polyanionic doping (BO_3^{3-}, PO_4^{3-}, and SiO_3^{2-}) of nanosized Li_xMnO_2

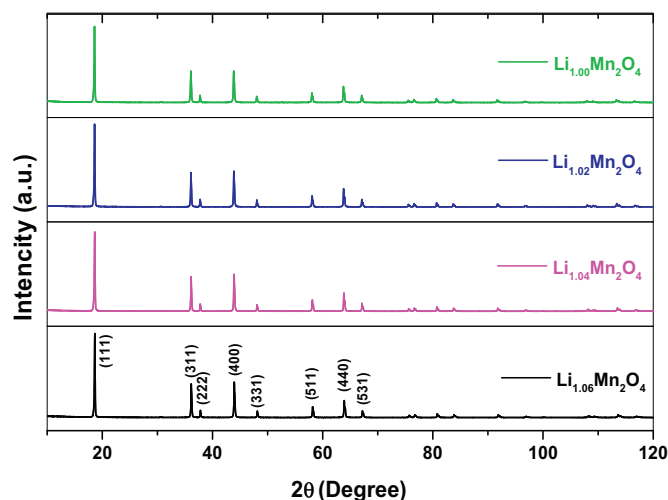**Fig. 1.** XRD patterns of $Li_xMn_2O_4$ synthesized at various Li concentration (x = 1.0, 1.02, 1.04, 1.06).

was found to be effective in improving the cycle stability and high-rate discharge capability, via a low-temperature redox soft-chemistry route with protection by liquid olefins [18]. Wu et al. found that the spectral features of the cation-doped spinels are sensitive to the dopant content, the structure of the MO_6 (M = Li, Mn, Cr) groups, the charge distribution and the average oxidation state of Mn [19].

In this work, we systematically studied $Li_xMn_2O_4$ with different Li concentrations, synthesized under the same experimental conditions and using the same precursors prepared by the solid-state reaction method. The structures, morphology, crystal plane spacing, and Mn valence state of the $Li_xMn_2O_4$ were investigated by X-ray diffraction (XRD), scanning electron microscopy (SEM), transmission electron microscopy (TEM), and X-ray photoelectron spectroscopy (XPS), respectively. Furthermore, the initial discharge curve measurements, cycling tests, rate capability measurements, and electrochemical impedance spectroscopy (EIS) were performed to investigate the electrochemical performance of the different $Li_xMn_2O_4$ samples. The results indicated that the changes in Mn^{4+}, R_{sf}, and R_{ct} with the increase in Li content are related to the changes in the second phase in $LiMn_2O_4$.

2. Experimental

To synthesize $LiMn_2O_4$, a mixture of as-prepared Mn_3O_4 and Li_2CO_3 (mole ratios of Li/Mn = 1.0:2, 1.02:2, 1.04:2, 1.06:2) was mixed with alcohol in an agate mortar, calcined at 500 °C for 5 h, and then sintered at 750 °C for 10 h. Finally, a black powder ($LiMn_2O_4$) was obtained. Pristine Mn_3O_4 and Li_2CO_3 were bought from industrial manufactures. The technological composition for each metal in $Li_xMn_2O_4$ (x = 1.0, 1.02, 1.04, 1.06) is the same as the stoichiometry determined by inductively coupled plasma (ICP) spectroscopy.

The structure of the resulting $LiMn_2O_4$ was characterized by powder XRD (D/Max2500PC, Japan) with Cu Kα radiation, a graphite monochromator, a tube voltage of 30 kV, a tube current of 100 mA, and a step size of 0.02° from 10° to 120°. The morphology and microstructure of the samples were studied using field emission scanning electron microscopy (FESEM, Nova Nano SEM450, USA). XPS measurements were performed using a Thermo Scientific ESCALAB 250 XI with a monochromatic Al Kα (1350.08 eV) anode (250 W, 10 kV, 30 mA). TEM measurements were performed using a JEM-2100F (200 V). The as-synthesized $LiMn_2O_4$, carbon black, and polyvinylidene fluoride were mixed with a weight ratio of 85:10:5 in *N*-methyl-2-pyrrolidone to form a slurry. The slurry was coated onto an aluminum foil and then dried in a vacuum oven at 120 °C for 12 h. The electrolyte was a 1 M $LiPF_6$ solution in ethylene carbonate, dimethyl carbonate, and ethyl methyl carbonate in a 1:1:1 volume ratio. A Cellgard 2400 membrane was used as the electrode separator. Then, the synthesized cathode materials were made into CR2016 coin cells with a metallic lithium plate as the counter electrode. Charge/discharge tests were performed over a voltage range of 3.0–4.3 V with a battery test system (LAND-CT2001A, China). Electrochemical impedance spectroscopy was performed using an impedance analyzer (Zahner Elektrik IM6, Germany) over a frequency range of 100 mHz to 100 kHz with an amplitude of 10 mV.

3. Results

Fig. 1 shows XRD patterns of the $Li_xMn_2O_4$ (x = 1.0, 1.02, 1.04, 1.06) samples. Fig. 2 shows an XRD pattern, with its refinement, for the sample prepared with a Li concentration of 1.0. The XRD patterns shown in Fig. 1 match well with the standard state of spinel $LiMn_2O_4$. Table 1 shows that the lithium ions occupy the tetrahedral (8a) sites and the manganese ions reside in the octahedral (16d) sites [20]. The strong and sharp reflection peaks in Fig. 1 suggest that the as-prepared $LiMn_2O_4$ was well crystallized. In our samples, the intensity ratio of the (311)/(400) peaks first decreased, and then increased with increasing lithium content. The intensity ratio of the (311)/(400) peaks is in the range 93.6%–99.9%. Furthermore, Wang et al. [21] confirmed that the intensity ratio of the (311)/(400) peaks relates to good cyclability. These parameters can be used to forecast the battery performance of $LiMn_2O_4$ spinel materials. Therefore, the electrochemical performance for our samples can be predicted to first decrease and then increase with increasing Li content.

Fig. 3 shows the morphologies and microstructures of $LiMn_2O_4$ samples. It can be seen that $LiMn_2O_4$ powders have a typical cubic spinel structure and the estimated primary particle size is about 0.1–0.7 μm in diameter, in the range of submicrocrystal. No significant changes were observed between the four samples shown in Fig. 3, indicating that a small amount of excessive doping of lithium source has no effect on the morphology of $LiMn_2O_4$ materials produced using the solid-state method.

Fig. 4 shows the XPS spectra of Mn $2p_{3/2}$ core-levels of $Li_xMn_2O_4$ samples that result from the spin-orbit splitting. The Mn $2p_{3/2}$ XPS binding energy for Mn^{3+} and Mn^{4+} is located at 641.7 eV (Mn_2O_3) and 642.6 eV (MnO_2), respectively. After peak-fitting; binding energy,
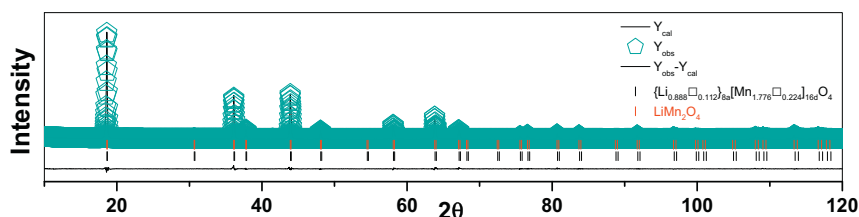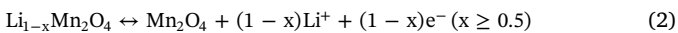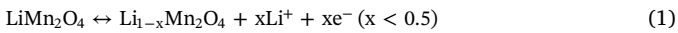
Fig. 2. Rietveld refinement of XRD patterns of $LiMn_2O_4$.

Table 1

The structural parameters determined for the $Li_xMn_2O_4$ (x = 1.0, 1.02, 1.04, 1.06) materials from the refinement of the XRD data. ($Li_2Mn_4O_9$ is an abbreviated form of $\{Li_{0.888}\square_{0.112}\}_{8a}[Mn_{1.776}\square_{0.224}]_{16d}O_4$; $Li_2Mn_3O_7$ is an abbreviated form of $\{Li_{0.864}\square_{0.136}\}_{8a}[Mn_{1.704}Li_{0.288}]_{16d}O_4$).

	$LiMn_2O_4$		$Li_{1.02}Mn_2O_4$		$Li_{1.04}Mn_2O_4$		$Li_{1.06}Mn_2O_4$	
	$LiMn_2O_4$	$Li_2Mn_4O_9$	$LiMn_2O_4$	$Li_2Mn_3O_7$	$LiMn_2O_4$	$Li_2Mn_3O_7$	$LiMn_2O_4$	$Li_2Mn_3O_7$
Lattice constants								
a(Å)	8.24474(8)	8.2382(6)	8.24489(7)	8.2384(5)	8.23704(7)	8.2298(6)	8.22986(9)	8.2216(6)
Cell volume (Å^3)	560.442(0.009)	559.103(0.071)	560.472(0.008)	559.158(0.065)	558.874(0.008)	557.392(0.069)	557.413(0.010)	555.742(0.075)
Structure parameters								
R_p	6.69		7.10		7.37		7.31	
R_{wp}	10.0		10.2		10.7		10.9	
Li_{8a}								
X	0.12500(0)	0.12500(0)	0.12500(0)	0.12500(0)	0.12500(0)	0.12500(0)	0.12500(0)	0.12500(0)
Y	0.12500(0)	0.12500(0)	0.12500(0)	0.12500(0)	0.12500(0)	0.12500(0)	0.12500(0)	0.12500(0)
Z	0.12500(0)	0.12500(0)	0.12500(0)	0.12500(0)	0.12500(0)	0.12500(0)	0.12500(0)	0.12500(0)
B	0.353(187)	0.500(0)	0.361(194)	0.500(0)	0.350(216)	0.500(0)	0.096(219)	0.500(0)
SOF	1.00000(0)	0.88814(0)	1.00000(0)	0.86414(0)	1.00000(0)	0.86414(0)	1.00000(0)	0.86414(0)
Mn_{16d}								
X	0.50000(0)	0.50000(0)	0.50000(0)	0.50000(0)	0.50000(0)	0.50000(0)	0.50000(0)	0.50000(0)
Y	0.50000(0)	0.50000(0)	0.50000(0)	0.50000(0)	0.50000(0)	0.50000(0)	0.50000(0)	0.50000(0)
Z	0.50000(0)	0.50000(0)	0.50000(0)	0.50000(0)	0.50000(0)	0.50000(0)	0.50000(0)	0.50000(0)
B	0.384(15)	0.500(0)	0.387(15)	0.500(0)	0.445(19)	0.500(0)	0.344(24)	0.500(0)
SOF	1.0000(0)	0.88815(0)	1.0000(0)	0.85214(0)	1.0000(0)	0.85214(0)	1.0000(0)	0.85214(0)
Li_{16d}								
X			0.50000(0)		0.50000(0)		0.50000(0)	
Y			0.50000(0)		0.50000(0)		0.50000(0)	
Z			0.50000(0)		0.50000(0)		0.50000(0)	
B			0.500(0)		0.500(0)		0.500(0)	
SOF			0.14402(0)		0.14402(0)		0.14402(0)	
O_{32e}								
X	0.26184(14)	0.26619(216)	0.26159(15)	0.27836(270)	0.26189(15)	0.27450(223)	0.26149(16)	0.26773(244)
Y	0.26184(14)	0.26619(216)	0.26159(15)	0.27836(270)	0.26189(15)	0.27450(223)	0.26149(16)	0.26773(244)
Z	0.26184(14)	0.26619(216)	0.26159(15)	0.27836(270)	0.26189(15)	0.27450(223)	0.26149(16)	0.26773(244)
B	1.152(43)	0.500(0)	1.131(45)	0.500(0)	0.906(48)	0.500(0)	0.759(50)	0.500(0)
SOF	1.00000(0)	1.00000(0)	1.00000(0)	1.00000(0)	1.00000(0)	1.00000(0)	1.00000(0)	1.00000(0)

cation distribution of Mn^{3+} and Mn^{4+}, and average valance of Mn could be obtained (see Table 2). The data showed that there were both Mn^{3+} and Mn^{4+} in the samples. Additionally, the Mn^{4+} content gradually decreased from 84.80% to 82.62% and then increased to 88.98% from 82.62%, as shown in Fig. 5. As a consequence, the average valency of Mn decreased from 3.8480 to 3.8262, and then increased to 3.8898 from 3.8262 with increasing lithium content.

Fig. 6 shows the charge-discharge curves for 3.0–4.3 V at a rate of 0.5C. The following cyclic tests and rate capability tests were demonstrated using the same coin cell. There are two voltage plateaus: one near 4.0 V and the other near 4.1 V, which indicates that Li^+ deintercalation from the oxide occurred step-by-step (as shown in Eqs. (1) and (2)) [22,23].

$$LiMn_2O_4 \leftrightarrow Li_{1-x}Mn_2O_4 + xLi^+ + xe^- \ (x < 0.5) \tag{1}$$

$$Li_{1-x}Mn_2O_4 \leftrightarrow Mn_2O_4 + (1-x)Li^+ + (1-x)e^- \ (x \geq 0.5) \tag{2}$$

The $LiMn_2O_4$ prepared at the Li concentration 1.06 presents the highest discharge capacity (135.3 mAh/g), which results from its higher crystallized microstructure. Similar discharge capacities of 126 mAh/g and 126.7 mAh/g were observed for Li concentrations of 1.02 and 1.04, respectively.

Fig. 7 shows the rate capability of $LiMn_2O_4$ samples at 25 °C. The rate capability was investigated at different C-rates (current densities). For each 5-cycle average, the charge and discharge process was performed at the same C-rate: between 4.3 V and 3.0 V at room temperature. As the current densities increased from 0.1C to 2C, a large

decrease in the discharge capacity was observed for the $LiMn_2O_4$ sample, which results from the increased polarization of the batteries due to limited Li^+ ion diffusion during cycling. Between 4.3 V and 3.0 V, $Li_{1.06}Mn_2O_4$ had a discharge capacity of 130.6, 127, 135.3, 115.6, and 94 mAh/g at 0.1, 0.2, 0.5, 1 and 2 C, respectively. These results indicate that the $Li_{1.06}Mn_2O_4$ sample has the best rate capability.

To further study the electrochemical behavior of the $LiMn_2O_4$ products, electrochemical impedance spectroscopy (EIS) measurements were conducted on the samples after 5 cycles at a rate of 0.1 C at a fully discharged state (see Fig. 8). It is clear that each spectrum consists of one obvious depressed semicircle in the high-to-medium frequency and another straight line in the low frequency. The equivalent circuit shown in Fig. 8 was used to fit the EIS data. In this circuit, R_e is the electrolyte resistance and electrode resistance. R_{sf} is the resistance of Li^+ ions through the SEI film. The semicircle is associated with the resistance resulting from lithium ion diffusion in the surface layer, representing the charge-transfer resistance (R_{ct}), and the slope in the low-frequency region is related to lithium ion diffusion in the bulk material. The plot of the real part of the impedance, Z′ vs. $\omega^{-0.5}$, at the low frequency region for the synthesized $Li_xMn_2O_4$ samples of various Li concentrations (x = 1.0, 1.02, 1.04, 1.06) is displayed in Fig. 9. R_e, R_{sf}, R_{ct}, and D_{Li^+} values simulated by ZSimpWin software for $LiMn_2O_4$ samples are listed in Table 3. The Li-ion diffusion coefficient (D_{Li^+}) in the cathode is estimated according to Eq. (3):

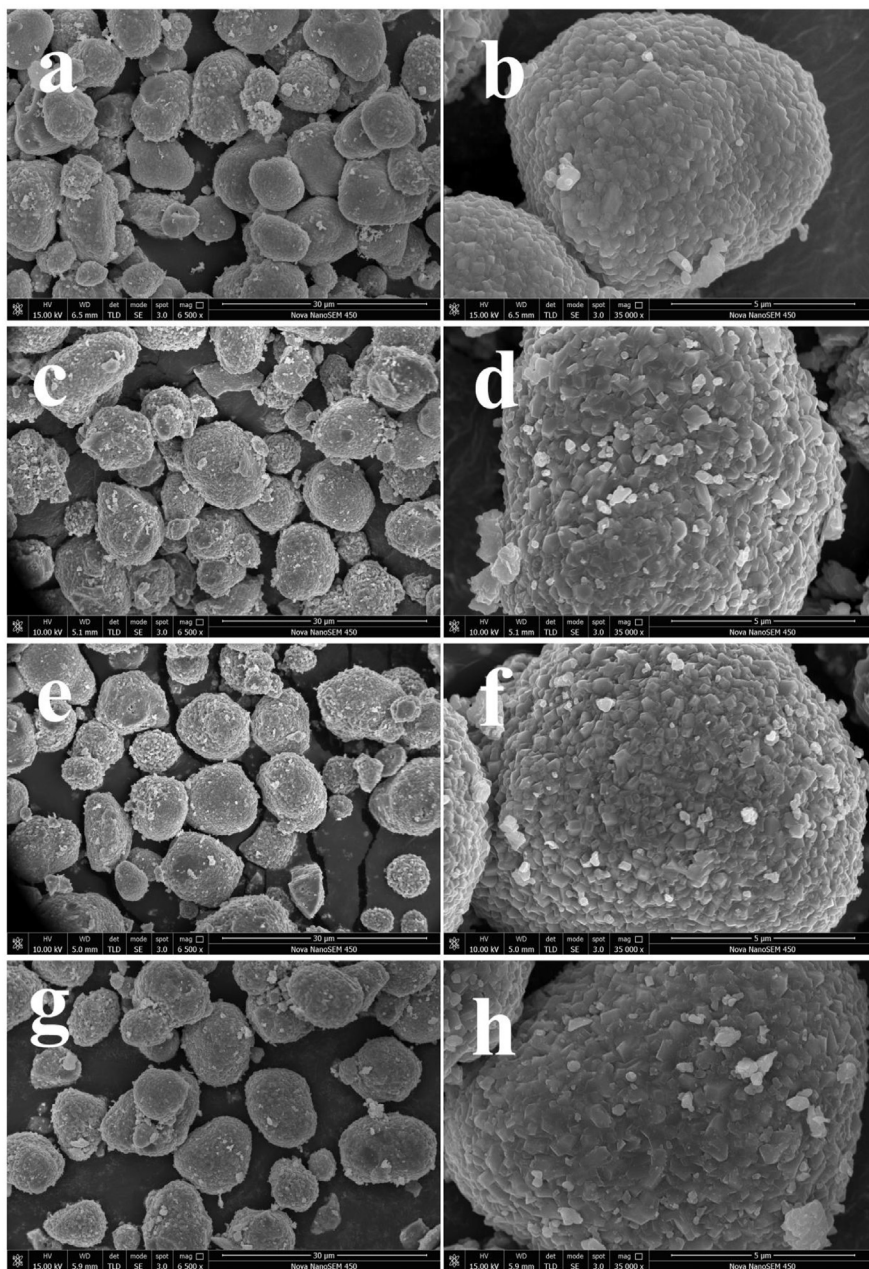$$D_{Li^+} = \frac{R^2T^2}{2A^2n^4F^4C^2\sigma^2} \tag{3}$$

Fig. 3. SEM micrographs of $Li_xMn_2O_4$ samples synthesized at various Li concentration (x = 1.0, 1.02, 1.04, 1.06) (a,b): $LiMn_2O_4$; (c,d): $Li_{1.02}Mn_2O_4$; (e,f): $Li_{1.04}Mn_2O_4$; (g,h): $Li_{1.06}Mn_2O_4$.

where R is the gas constant, T the absolute temperature, A the surface area of the electrode, n the number of electrons per molecule during electrode reaction, F the Faraday constant, C the concentration of Li-ion in electrode, and σ the Warburg coefficient. σ can be obtained according to Eq. (4):

$$Z' = R_e + R_{ct} + \sigma\,\omega^{-1/2} \qquad (4)$$

where ω is the angular frequency. The Warburg coefficient (σ) is the slope of Z' vs. $\omega^{-1/2}$ after linear fitting. Li-ion diffusion coefficient (D_{Li}^+) is estimated from Eqs. (3) and (4) [24]. The highest R_e, R_{sf}, and R_{ct} values were observed at 5.912 Ω, 37.84 Ω, and 133.1 Ω, respectively, when the Li concentration is 1.02. As shown in Table 3, the D_{Li}^+ gradually decreased from $5.94 \times 10^{-16}\,cm^2\,s^{-1}$ to $5.56 \times 10^{-16}\,cm^2\,s^{-1}$, and then increased from $5.56 \times 10^{-16}\,cm^2\,s^{-1}$ to $1.739 \times 10^{-15}\,cm^2\,s^{-1}$, when the Li concentration increased from 1.00 to 1.06. The high diffusion coefficient is related to the better electrochemical performance, which is inversely proportional to R_{sf} and R_{ct}. In addition, Fig. 10 shows that the R_{ct} values gradually increased from 58.33 Ω to 133.1 Ω, and then decreased to 68.79 Ω from 133.1 Ω, when the Li concentration increased from 1.00 to 1.06. The R_{sf} values also increased from 25.67 Ω to 37.84 Ω and then decreased from 37.84 Ω to 16.69 Ω, when the Li concentration increased from 1.00 to 1.06 (see Fig. 10).

4. Discussion

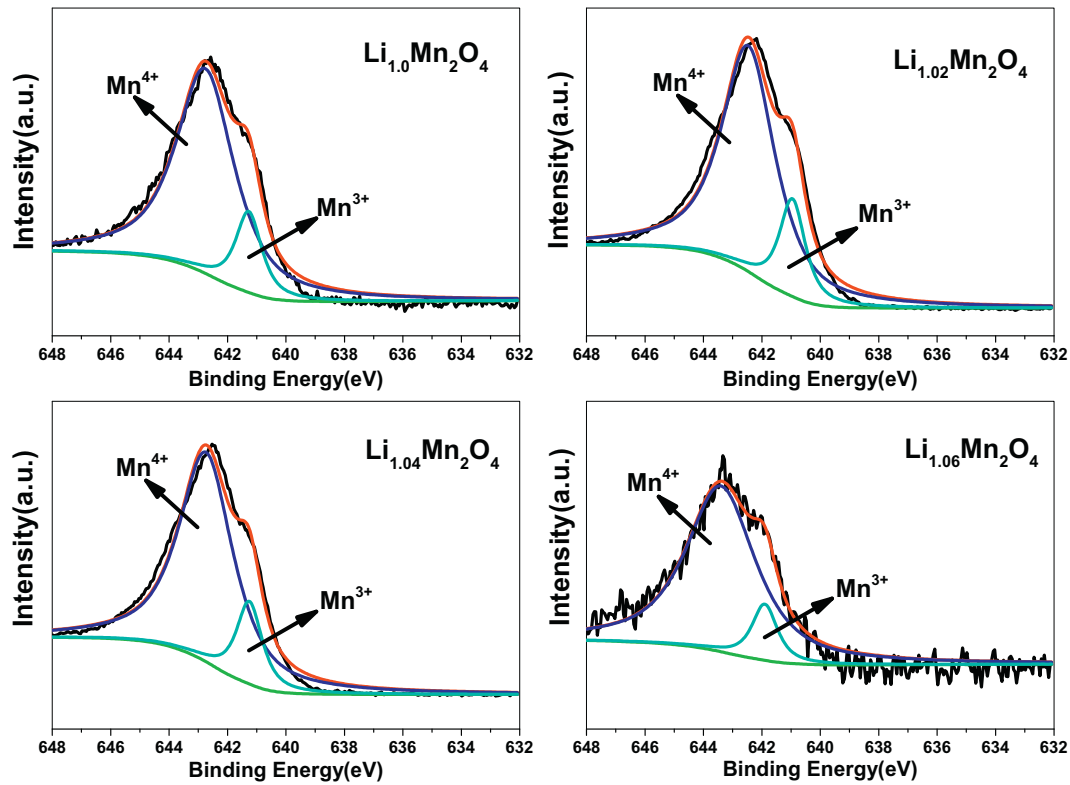Fig. 11 shows TEM images of the $Li_{1.06}Mn_2O_4$ sample. Fig. 11(a)

Fig. 4. Deconvoluted profile of specific Mn $2p_{3/2}$ XPS spectra of $Li_xMn_2O_4$ (x = 1.0, 1.02, 1.04, 1.06).

Table 2
Binding energy, cation distribution, and average valence of Mn from XPS (Mn-$2p_{3/2}$ spectra) of $LiMn_2O_4$ samples.

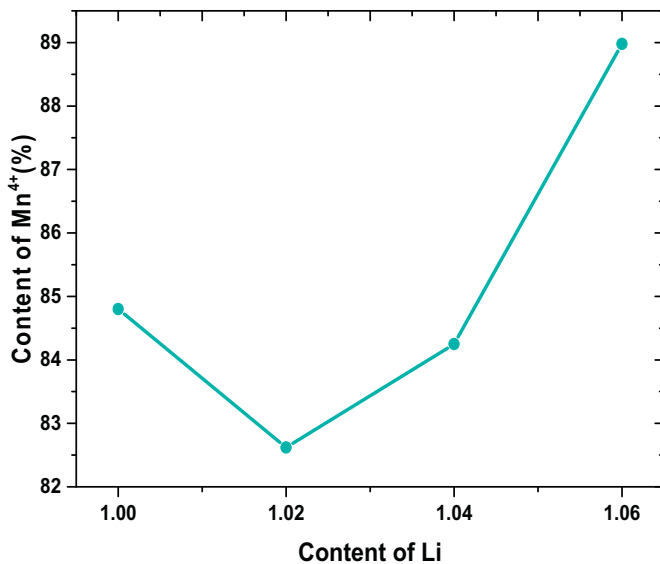| Sample	Binding energy(eV)		Cation distribution		Average valence
	Mn^{4+}	Mn^{3+}	Mn^{4+} (%)	Mn^{3+} (%)	Mn
Li1.00	642.758	641.273	84.80	15.20	3.8480
Li1.02	642.457	640.953	82.62	17.38	3.8262
Li1.04	642.732	641.251	84.25	15.75	3.8425
Li1.06	643.396	641.900	88.98	11.02	3.8898

Fig. 5. The Mn^{4+} content of $Li_xMn_2O_4$ samples with the various Li concentration (x = 1.0, 1.02, 1.04, 1.06).

shows the HRTEM image, Fig. 11(b) is the fast-Fourier transform (FFT) pattern in the [011] zone. As shown in Fig. 11(b), the far spot that is further away from (000) and the near spot that is nearer to (000) on the (400) plane indicate the spot splitting of the (400) plane. The spot splitting of the (400) plane leads to a reduction in the intensity of the (400) peak, which increases the intensity ratio of the (311)/(400) peaks, as shown in Fig. 1. The XRD pattern in Fig. 1 shows that the intensity ratio of the (311)/(400) peaks is between 93.6%–99.9%. By calculating the structure factor, the intensity of (311) and (400) peaks are obtained, and we then get the theoretical value of the intensity ratio of the (311)/(400) peaks of about 84% [21]. The difference between the experimental and theoretical values is due to the spot splitting of the (400) plane. Fig. 11(c) is the inverse FFT image and Fig. 11(d) and Fig. 11(e) show the far-spot imaging and the near-spot imaging in the inverse FFT image, which are basically complementary images. Ten layers of crystal faces perpendicular to the (400) direction were measured in Fig. 11(d) and (e) and the results are shown in Fig. 11(f) and (g). The results indicate that the crystal-plane spacing of the far-spot on the (400) plane is 0.196 nm, and the crystal plane spacing of the near-spot on the (400) plane is 0.204 nm, as shown in the inverse FFT image. Different crystal plane spacing in Fig. 11(c) and the spot splitting on the (400) plane in Fig. 11(b) indicate the existence of the second phase.

The second phase may be one of the following three structures: Xu et al. [25] pointed out that the dominant part of a given sample is the cubic spinel phase (Fd-3 m) with secondary tetragonal phases ($I4_1/$ amd), which have different lattice parameters. Oikawa et al. [26] showed that reflections of the LT phase in its neutron and X-ray diffraction patterns were indexed not on the basis of a tetragonal unit cell ($I4_1/amd$) but roughly as an orthorhombic one (space group Fddd), with lattice parameters a = 8.2797(2), b = 8.2444(3) and c = 8.1981(2) Å. In addition, Thackeray et al. [27] have proposed that the cation distributions in the structures were determined by neutron diffraction to be $\{Li_{0.85}\Upsilon_{0.15}\}_{8a}[Mn_{1.74}Li_{0.26}]_{16d}O_4$ and $\{Li_{0.89}\Upsilon_{0.11}\}_{8a}[Mn_{1.78}\Upsilon_{0.22}]_{16d}O_4$, which include $Li_2Mn_4O_9$ and $Li_2Mn_3O_7$, where 8a and 16d refer to the tetrahedral and octahedral
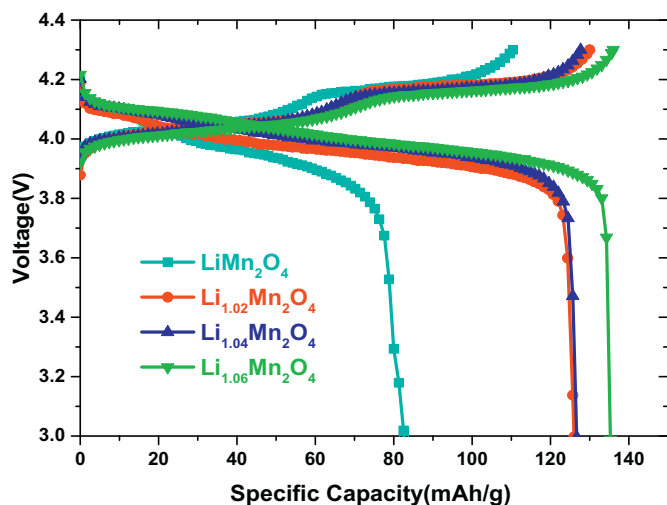
Fig. 6. The charge-discharge curves of $Li_xMn_2O_4$ samples with the various Li concentration (x = 1.0, 1.02, 1.04, 1.06) between 3.0 V to 4.3 V at a rate of 0.5C.

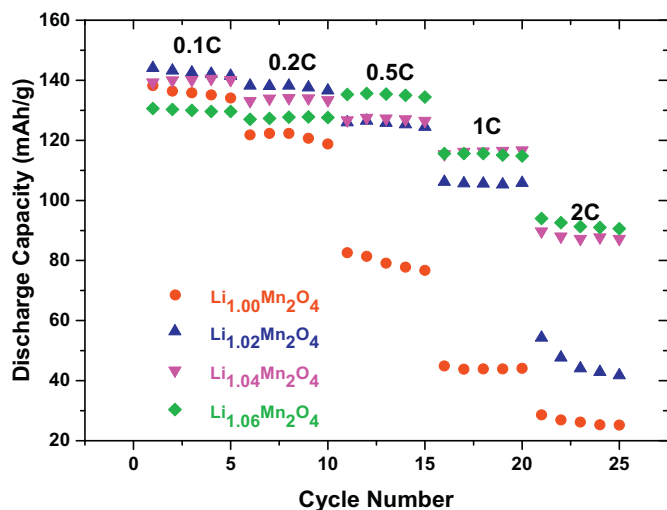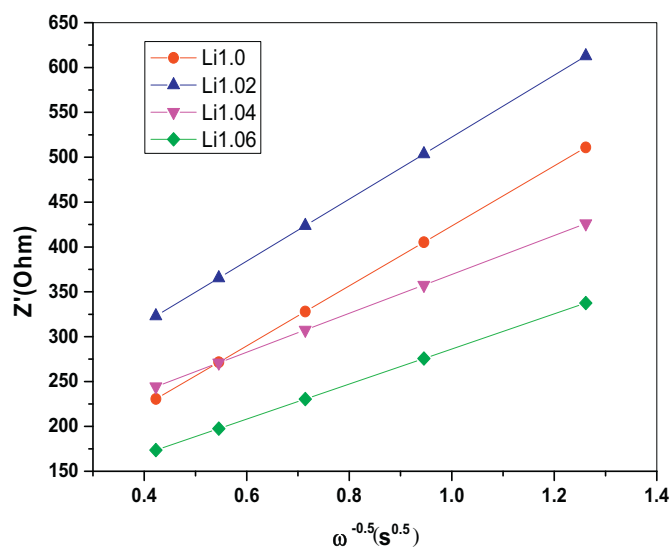**Fig. 7.** Rate capability of $Li_xMn_2O_4$ samples with the various Li concentration (x = 1.0, 1.02, 1.04, 1.06) at 25 °C.

Fig. 9. Z'vs.$\omega^{-0.5}$ plots at the low frequency region for the synthesized $Li_xMn_2O_4$ samples with the various Li concentration (x = 1.0, 1.02, 1.04, 1.06).

Table 3

R_e, R_{sf}, R_{ct}, and D_{Li}^+ for $Li_xMn_2O_4$ samples with the various Li concentration (x = 1.0, 1.02, 1.04, 1.06).

Sample	R_e (Ω)	R_{sf} (Ω)	R_{ct} (Ω)	D_{Li}^+ (cm^2 s^{-1})
Li1.00	5.258	25.67	58.33	5.94×10^{-16}
Li1.02	5.912	37.84	133.1	5.56×10^{-16}
Li1.04	5.006	30.39	117.4	1.415×10^{-15}
Li1.06	5.454	16.69	68.79	1.739×10^{-15}

sites of the prototypic spinel space group Fd-3 m, respectively. We used four methods to refine the structure of $LiMn_2O_4$. The refinement results indicated that, using this refinement method, the structure where the first phase is $LiMn_2O_4$ with the Fd-3 m space group and the second phase is $\{Li_{0.864}\Upsilon_{0.136}\}_{8a}[Mn_{1.704}Li_{0.288}]_{16d}O_4$ with the Fd-3 m space group had the lowest residual factor. However, refinement results of the single-phase with the Fd-3 m space group, a phase with Fd-3 m space group and the other phase with Fddd space group, and a phase with Fd-
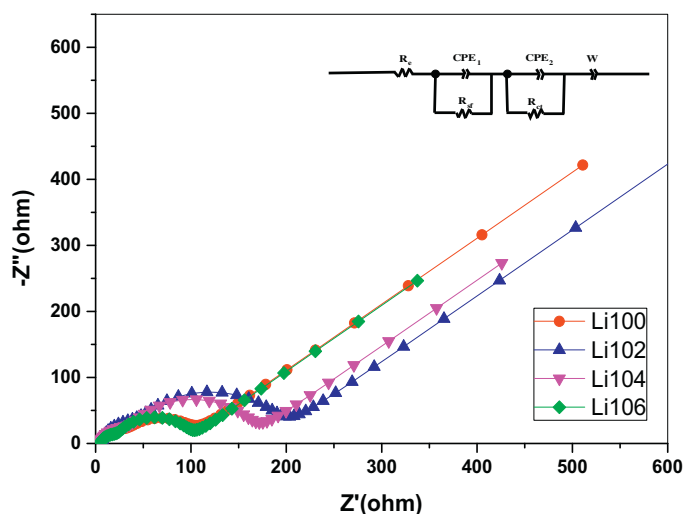

Fig. 8. Electrochemical impedance spectroscopy of the synthesized $Li_xMn_2O_4$ samples with the various Li concentration (x = 1.0, 1.02, 1.04, 1.06) with an amplitude of 10 mV.
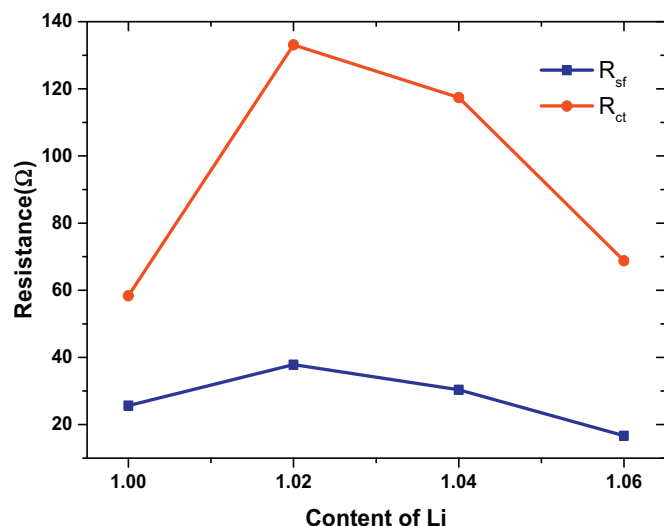
Fig. 10. The R_{sf} and R_{ct} values of $Li_xMn_2O_4$ samples with the various Li concentration (x = 1.0, 1.02, 1.04, 1.06).

3 m space group and the other phase with $I4_1/amd$ space group, had higher residual factor. Therefore, the second phase space group was the Fd-3 m space group. Meanwhile, thermogravimetric experiments showed oxygen excess in our samples, which indicated that the oxygen content in the second phase was high, so we determined that the second phase was dominated by Mn^{4+}. The second phase was $\{Li_{0.888}\Upsilon_{0.112}\}_{8a}[Mn_{1.776}\Upsilon_{0.224}]_{16d}O_4$, when the Li/Mn ratio was 1.0:2. The $\{Li_{0.888}\Upsilon_{0.112}\}_{8a}[Mn_{1.776}\Upsilon_{0.224}]_{16d}O_4$ gradually changed to $\{Li_{0.864}\Upsilon_{0.136}\}_{8a}[Mn_{1.704}Li_{0.288}]_{16d}O_4$, with the gradual increase of lithium content.

The $\{Li_{0.888}\Upsilon_{0.112}\}_{8a}[Mn_{1.776}\Upsilon_{0.224}]_{16d}O_4$ second phase was formed in $LiMn_2O_4$, when the Li/Mn ratio was 1.0:2. The $\{Li_{0.888}\Upsilon_{0.112}\}_{8a}[Mn_{1.776}\Upsilon_{0.224}]_{16d}O_4$ gradually changed to $\{Li_{0.864}\Upsilon_{0.136}\}_{8a}[Mn_{1.704}Li_{0.288}]_{16d}O_4$, with the gradual increase of lithium content. The total amount of the second phase decreased gradually, which meant the amount of Mn^{4+} gradually decreased, as shown in Fig. 5. Due to the existence of the second phase, the formation of a surface passivation film between the cathode material and the electrolyte is suppressed, thereby reducing the value of R_{ct} and R_{sf} [14]. When the lithium content increased from 1 to 1.02, the total amount of the second phase was reduced to the minimum, which made the values of R_{sf} and R_{ct} gradually increase to the maximum, as shown in Fig. 10. When the lithium content increased from 1.02 to 1.06, the amount of $\{Li_{0.864}\Upsilon_{0.136}\}_{8a}[Mn_{1.704}Li_{0.288}]_{16d}O_4$ increased gradually, which lead to an increase in Mn^{4+} and a decrease in R_{sf} and R_{ct}.

The results indicate that the rate capability of the $LiMn_2O_4$ samples evidently increases as the lithium content increases from 1.00 to 1.06, as shown in Fig. 7. Although R_{ct} and R_{sf} are very low when the Li content was 1.0, and the rate performance is poor, which is related to the Jahn-Teller effect [11]. Fig. 7 shows the rate capability of $LiMn_2O_4$ samples, where the results verify the prediction of the electrochemical performance in Fig. 1.

5. Conclusions

In this study, we systematically studied $Li_xMn_2O_4$ with different Li concentrations, synthesized under the same experimental conditions, using the same precursors prepared by solid-state reaction method. The TEM measurements showed different crystal plane spacing and spot splitting on the (400) plane, which indicated the existence of the second phase. The refinement results showed that the second phase space group has an Fd-3 m structure. Upon increasing of the Li content, the Mn^{4+} content first decreased and then increased, while the values of R_{ct} and R_{sf} first increased and then decreased, which are related to the transformation of the second phase in $LiMn_2O_4$. The rate capability of
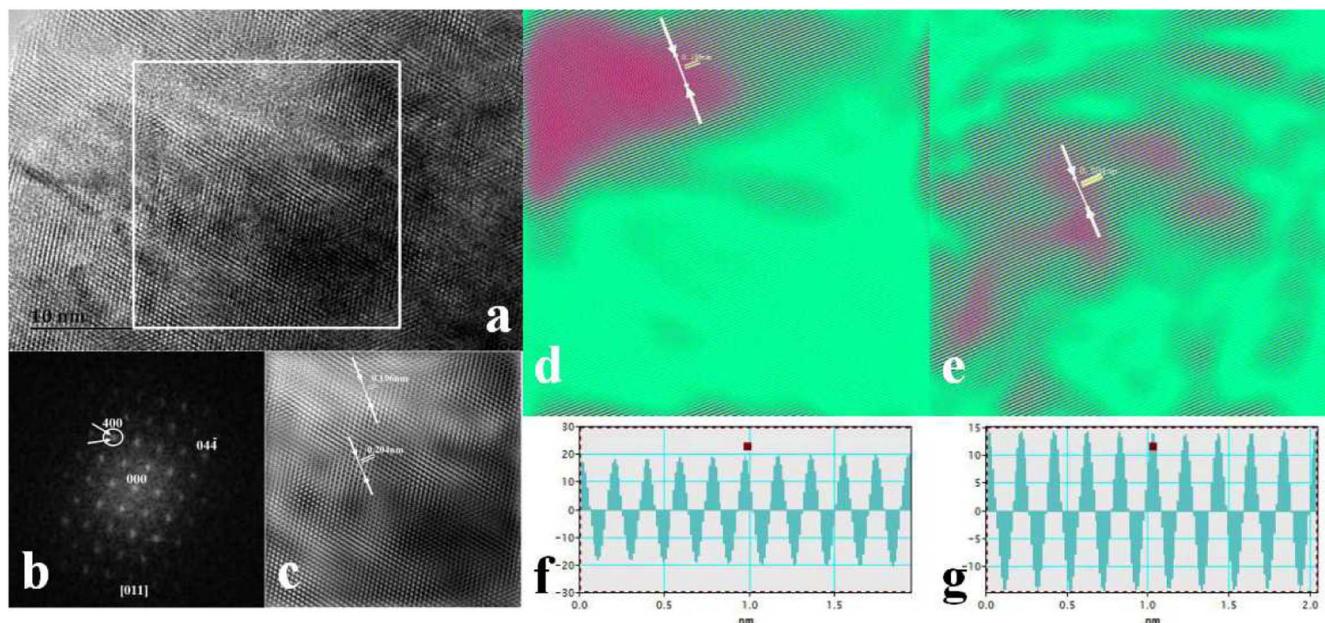

Fig. 11. The $Li_{1.06}Mn_2O_4$ sample of (a): HRTEM image, and the selected area is carried out the fast-Fourier transform(FFT); (b): the fast-Fourier transform(FFT) pattern in the [011] zone, the far spot that is further away from (000) and near spot that is nearer to (000) on the (400) plane indicate the spot splitting of the (400) plane; (c): inverse FFT image, and shows different crystal plane spacing; (d): the far-spot imaging in the inverse FFT image, and the results indicate that the crystal plane spacing of the far-spot on the (400) plane is 0.196 nm; (e): the near-spot imaging in the inverse FFT image, and the results indicate that the crystal plane spacing of the near-spot on the (400) plane is 0.204 nm; (f): crystal plane spacing of the far-spot imaging in (d), and (g): crystal plane spacing of the near-spot imaging in (e), and ten layers of crystal faces that perpendicular to the (400) direction are measured in Fig. 11(d) and Fig. 11(e) and the results are shown in Fig. 11(f) and Fig. 11(g).

the LiMn$_2$O$_4$ samples also increased as the Li content increased from 1.00 to 1.06.

References

[1] Q. Zhang, J. Mei, X. Wang, W. Fan, F. Wang, W. Lu, F. Tang, J. Alloys Compd. 606 (2014) 249–253.
[2] W. Tang, X.J. Wang, Y.Y. Hou, L.L. Li, H. Sun, Y.S. Zhu, Y. Bai, Y.P. Wu, K. Zhu, T.V. Ree, J. Power Sources 198 (2012) 308–311.
[3] S.N. Karthick, S.R.P. Gnanakan, A. Subramania, H.J. Kim, J. Alloys Compd. 489 (2010) 674.
[4] H. Yoshizawa, T. Ohzuku, J. Power Sources 174 (2007) 813–817.
[5] G.R. Hu, J.B. Jiang, Z.D. Peng, K. Du, Y. Gao, J. Duan, J. Nanosci. Nanotechnol. 13 (2013) 2262–2265.
[6] W. Choi, A. Manthiram, J. Electrochem. Soc. 153 (2006) A1760.
[7] R.J. Gummow, A. Dekock, M.M. Thackeray, Solid State Ionics 69 (1994) 59.
[8] J. Lu, C. Zhan, T. Wu, J. Wen, Y. Lei, A.J. Kropf, H. Wu, D.J. Miller, J.W. Elam, Y.-K. Sun, X. Qiu, K. Amine, Nat. Commun. 5 (2014) 5693.
[9] O.K. Park, Y. Cho, S. Lee, H.-C. Yoo, H.-K. Song, J. Cho, Olivine or spinel, Energy Environ. Sci. 4 (2011) 1621.
[10] Y. Shin, A. Manthiram, Electrochem. Solid-State Lett. 5 (3) (2002) A55.
[11] K.Y. Chung, K.-B. Kim, J. Electrochem. Soc. 149 (2002) A79.
[12] S.R. Das, et al., J. Power Sources 158 (1) (2006) 518–523.
[13] B.J. Kang, J.-B. Joo, J.K. Lee, J. Electroanal. Chem. 728 (2014) 34.
[14] C.-G. Han, et al., Electrochim. Acta 209 (2016) 225–234.
[15] Z. Bakenov, I. Taniguchi, Solid State Ionics 176 (2005) 1027.
[16] Q. Luo, A. Manthiram, J. Electrochem. Soc. 156 (2009) A84.
[17] Y.K. Sun, S.W. Oh, C.S. Yoon, H.J. Bang, J. Prakash, J. Power Sources 161 (2006) 19.
[18] Z. Su, S.H. Ye, T.Y. Yan, X.P. Gao, P.W. Shen, J. Electrochem. Soc. 155 (2008) A839.
[19] C. Wu, Z.X. Wang, F. Wu, L.Q. Chen, X.J. Huang, Solid State Ionics 144 (2001) 277–285.
[20] Y. Gao, J.R. Dahn, J. Electrochem. Soc. 143 (1996) 100–114.
[21] T.D. Wang, X.Y. Kang, H.B. Guo, Y. Han, Chin. J. Power Sources 29 (2005) 343–345.
[22] David R. Lide, Electrochemical series, Handbook of Chemistry and Physics, 88th ed., Chemical Rubber Company, 2007.
[23] X.M. Wu, X.B. Li, Z.B. Xiao, W.B. Yan, M.Y. Ma, Mater. Chem. Phys. 84 (2004) 182–186.
[24] H. Liu, C. Li, H.P. Zhang, L.J. Fu, Y.P. Wu, H.Q. Wu, J. Power Sources 159 (2006) 717–720.
[25] Z.L. Xu, J.B. Wang, X.J. Quan, S.J. Hu, Q.G. Wu, J. Power, Sources 248 (2014) 1201–1210.
[26] K. Oikawa, T. Kamiyama, F. Izumi, B.C. Chakoumakos, H. Ikuta, Solid State Ionics 109 (1998) 35–41.
[27] M.M. Thackeray, A.D. Kock, W. David, J. Mater. Res. Bulletin 28 (1993) 1041–1049.